PROCEEDINGS A

royalsocietypublishing.org/journal/rspa

Research

Cite this article: dos Santos FA, Favata A, Micheletti A, Paroni R, Picchi Scardaoni M. 2024 Programming quadric metasurfaces via infinitesimal origami maps of monohedral hexagonal tessellations: Part II. *Proc. R. Soc. A* **480**: 20230449.
https://doi.org/10.1098/rspa.2023.0449

Received: 20 June 2023
Accepted: 9 January 2024

Subject Areas:
applied mathematics, structural engineering, mechanics

Keywords:
metasurface, tessellation, morphing structure, rigid microstructure, three-dimensional printing

Author for correspondence:
Marco Picchi Scardaoni
e-mail: marco.picchiscardaoni@ing.unipi.it

Downloaded from https://royalsocietypublishing.org/ on 27 February 2024

Programming quadric metasurfaces via infinitesimal origami maps of monohedral hexagonal tessellations: Part II

Filipe A. dos Santos[1], Antonino Favata[2], Andrea Micheletti[3], Roberto Paroni[4] and Marco Picchi Scardaoni[4]

[1]CERIS-NOVA, Department of Civil Engineering, NOVA School of Science and Technology, Universidade NOVA de Lisboa, Caparica, Portugal
[2]Department of Structural and Geotechnical Engineering, Sapienza University of Rome, Rome, Italy
[3]Dipartimento di Ingegneria Civile e Ingegneria Informatica, University of Rome Tor Vergata, Rome, Italy
[4]Dipartimento di Ingegneria Civile e Industriale, Università di Pisa, Pisa, Italy

FAdS, 0000-0002-5815-4622; AF, 0000-0003-2760-8190; AM, 0000-0001-7842-5912; RP, 0000-0003-3040-0112; MPS, 0000-0003-1348-676X

In Part I of this study, it was shown that all the three known types of monohedral hexagonal tessellations of the plane, those composed of equal irregular hexagons, have just a single deformation mode when tiles are considered as rigid bodies hinged to each other along the edges. A gallery of tessellated plates was simulated numerically to demonstrate the range of achievable deformed shapes. In Part II, the displacement field was first derived and a continuous interpolant for each type of tessellated plate. It turns out that all corresponding metasurfaces are described by quadrics. Afterwards, a parametric analysis was carried out to determine the effect of varying angles and edge lengths on the curvature, and the values of the geometric Poisson ratio of the plates. Finally, a method of fabrication is proposed based on the additive manufacturing of stiff tiles of negligible deformability and flexible connectors. Using this modular technique, it is possible to join together different monohedral tessellated plates able

THE ROYAL SOCIETY PUBLISHING

© 2024 The Author(s) Published by the Royal Society. All rights reserved.

Downloaded from https://royalsocietypublishing.org/ on 27 February 2024

to deform into piece-wise quadrics. The nodal positions in the deformed configuration of the realized plates are measured after enforcing one principal curvature to assume a chosen value. The estimate of the other principal curvature confirms the analytical predictions. The presented tessellated plates permit to realize doubly curved shape-morphing metasurfaces with assorted shapes, which also can feature a certain surface roughness, and they can be employed in all applications demanding high surface accuracy and few actuators or just one.

1. Introduction

We refer the reader to Part I of this report [1] to find the background information, the motivation and the goal of our investigation, together with the related literature survey (table 1).

After proving in Part I that each type (Type 1, 2, 3) of tiled plates based on monohedral hexagonal tessellations possesses just one deformation mode, we begin Part II by presenting the derivation of the displacement field of the plates and of a continuous interpolant of their deformed configuration. Such an interpolant turned out to be a quadric whose geometric properties depend on those of the chosen tile. Different results were found for Type 1 and Type 2, in which the Gaussian curvature can be positive, negative or null, and for Type 3 plates, in which the Gaussian curvature is always non-negative with equal principal curvatures.

A parametric analysis was conducted to evaluate the effects of varying the edges lengths and the angles of a tile on the directional curvature of the corresponding metasurface, also in relation to the geometric Poisson ratio, defined here as the negative of the ratio between the maximum and minimum principal curvatures.

Subsequently, it is presented the experimental testing of physical models realized by assembling additively manufactured stiff tiles of negligible deformability with soft connectors. Three cases were examined for the basic tile, the regular hexagon, the hourglass shape and the arrow head shape, which correspond to metasurfaces with synclastic, anticlastic and monoclastic shapes, respectively. Measurements were collected by laser scanning the realized plates after enforcing one of their principal curvatures to assume a given value by using an arched beam in contact with the plate. We found that the estimate of the other principal curvature obtained in the experiments was in excellent agreement with the analytical values.

The implications of our findings, together with some considerations on future work, are discussed in the last section of this report.

2. Kinematics of monohedral hexagonal tessellations

We start our analysis by recalling some results derived in the companion paper. We denote by $\mathbb{R}^3$ the three-dimensional Euclidean space and we endow it with a right-handed orthonormal basis $\{\mathbf{e}_1, \mathbf{e}_2, \mathbf{e}_3\}$. We consider mechanical metasurfaces composed of rigid tiles. Let $\mathcal{T} = \{\tau^{(i)}\}_{i=1}^{N}$ be a finite family of closed sets (the regions occupied by the tiles), of $\mathbb{R}^3_0 = \{\mathbf{x} \in \mathbb{R}^3 : \mathbf{x} \cdot \mathbf{e}_3 = 0\}$, with disjoint interiors and let $\mathbf{u} : \cup_{i=1}^{N} \tau^{(i)} \to \mathbb{R}^3$ be a Lipschitz map. We say that the pair $(\mathcal{T}, v)$ is an *infinitesimal origami map* if $\mathbf{u}$ is affine on each $\tau^{(i)}$, $i = 1, \ldots, N$, and $\nabla \mathbf{u}(\mathbf{x})$ is a skew-symmetric tensor for almost every $\mathbf{x} \in \cup_{i=1}^{N} \tau^{(i)}$. If the tile undergoes an infinitesimal origami map, the displacement $\mathbf{u}^{(1)}(\mathbf{x}) \in \mathbb{R}^3$ of the point $\mathbf{x} \in \tau^{(1)}$ is given by

$$\mathbf{u}^{(1)}(\mathbf{x}) = \mathbf{u}^{(1)}(\mathbf{x}_0^{(1)}) + \mathbf{W}^{(1)}[\mathbf{x} - \mathbf{x}_0^{(1)}], \tag{2.1}$$

where $\mathbf{x}_0^{(1)}$ is a generic point of the tile, $\mathbf{W}^{(1)}$ is a skew-symmetric tensor. If two tiles are connected, we proved that the following condition holds:

$$\mathbf{W}^{(1)} - \mathbf{W}^{(2)} = \varphi^{\{1,2\}}\, \mathbf{e}_3 \otimes \mathbf{n}^{(1,2)}, \tag{2.2}$$

Downloaded from https://royalsocietypublishing.org/ on 27 February 2024

Table 1. Nomenclature.

$\mathbf{e}_1, \mathbf{e}_2, \mathbf{e}_3$	= canonical basis of $\mathbb{R}^3$
$\mathbf{d}_1, \mathbf{d}_2$	= (covariant) directors spanning the monohedral tessellation lattice
$\mathbf{d}^1, \mathbf{d}^2$	= contravariant directors
$\tau^{(i)}$	= region occupied by the ith tile
$\tau^{(i,j)}$	= translated tile
$\mathcal{T}$	= tessellation
$\mathbf{n}^{(i,j)}$	= unit normal vector to the segment shared by tiles i and j
$\mathbf{t}^{(i,j)}$	= unit tangent vector to the segment shared by tiles i and j
$\mathbf{u}$	= displacement
w_0	= continuous interpolant of $\mathbf{u} \cdot \mathbf{e}_3$
$\mathbf{x}$	= point in $\mathbb{R}^3$
$\mathbf{W}^{(i)}$	= skew-symmetric tensor for $\tau^{(i)}$
$\mathbf{W}^{(i,j)}$	= skew-symmetric tensor for $\tau^{(i,j)}$
$\boldsymbol{\omega}^{(i)}$	= axial vector of $\mathbf{W}^{(i)}$
$\varphi^{\{i,j\}}$	= relative rotation between tiles i and j
α	= interior angle in a polygon
$\alpha^{(i,j)}$	= angle between $\mathbf{e}_1$ and $\mathbf{t}^{(i,j)}$
ℓ	= side length
ϱ	= geometric Poisson ratio
$\mathbf{K}$	= curvature tensor of the monohedral tessellation
$\cdot$	= canonical inner product in $\mathbb{R}^3$
$\wedge$	= canonical exterior product in $\mathbb{R}^3$
$\otimes$	= dyadic (tensor) product
$\delta_{\alpha\beta}$	= Kronecker's delta

where $\varphi^{\{i,j\}}$ denotes the relative rotation between the tiles $\tau^{(i)}$ and $\tau^{(i)}$, and $\mathbf{n}^{(i,j)}$the normal that goes from $\tau^{(i)}$ to $\tau^{(j)}$.

If three tiles are considered, by applying (2.2) three times we have that

$$\begin{cases} \mathbf{W}^{(1)} - \mathbf{W}^{(2)} = \varphi^{\{1,2\}}\, \mathbf{e}_3 \otimes \mathbf{n}^{(1,2)}, \\ \mathbf{W}^{(2)} - \mathbf{W}^{(3)} = \varphi^{\{2,3\}}\, \mathbf{e}_3 \otimes \mathbf{n}^{(2,3)}, \\ \mathbf{W}^{(3)} - \mathbf{W}^{(1)} = \varphi^{\{3,1\}}\, \mathbf{e}_3 \otimes \mathbf{n}^{(3,1)}. \end{cases}$$

In part I, we have proved that

$$\varphi^{\{2,3\}} = -\varphi^{\{3,1\}} \frac{\sin(\alpha^{(3,1)} - \alpha^{(1,2)})}{\sin(\alpha^{(2,3)} - \alpha^{(1,2)})} \quad \text{and} \quad \varphi^{\{1,2\}} = \varphi^{\{3,1\}} \frac{\sin(\alpha^{(3,1)} - \alpha^{(2,3)})}{\sin(\alpha^{(2,3)} - \alpha^{(1,2)})}. \tag{2.3}$$

The meaning of the symbols is clarified in figure 1.

We say a tessellation of $\mathbb{R}^3_0$ is *monohedral* if all tiles are congruent. We call the basic tile *monotile*. The tessellation is then obtained by rotations, reflections and translations of the monotile. It has been shown [2,3] that there exist exactly three types of hexagonal, convex monotiles, reported in figure 2.

In the companion paper, we have shown that assuming the tessellation to have degree three (every interior vertex of the tessellation is in common to three tiles), and $|\alpha_i| \neq \{0, \pi\}$, then the

Downloaded from https://royalsocietypublishing.org/ on 27 February 2024

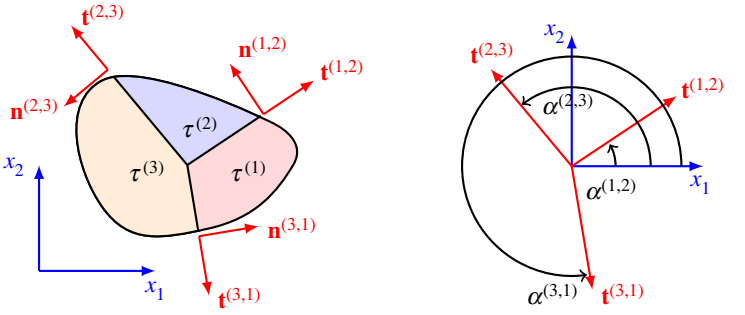

Figure 1. Geometry of three adjacent tiles.

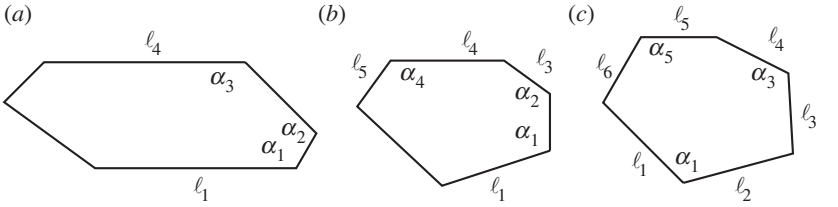

Figure 2. Types of hexagonal monotiles. Type 1: $\alpha_1+\alpha_2+\alpha_3=2\pi$, $\ell_1=\ell_4$. Type 2: $\alpha_1+\alpha_2+\alpha_4=2\pi$, $\ell_1=\ell_4$, $\ell_3=\ell_5$. Type 3: $\alpha_1=\alpha_3=\alpha_5=\frac{2}{3}\pi$, $\ell_1=\ell_2$, $\ell_3=\ell_4$, $\ell_5=\ell_6$. (*a*) Type 1, (*b*) Type 2 and (*c*) Type 3.

tessellations obtained by the three types of hexagonal monotiles have (under some additional conditions for the Type 2 case) one degree of freedom. Such a result is valid also for the concave counterpart of the three types.

3. Displacements of the periodic tessellations

In the companion paper, we conducted a comprehensive exploration of the degrees of freedom of metasurfaces fabricated using the three aforementioned hexagonal tessellation types. Building upon this foundation, our current focus shifts towards the derivation of the displacement field and the introduction of a systematic methodology for attaining a macroscale description of the displacement field through a continuous interpolant.

(a) Type 1

To describe the configurations of Type 1, we need seven parameters. We take the four angles, α, β, γ and δ, as depicted in figure 3*a*, and three lengths

$$CD = AF = EL = GH = a, \quad ED = FG = b, \quad EF = c.$$

As it should be clear from the figure, the angles α and β, as well as γ and δ, should satisfy some constraints in order to avoid unbounded tiles or tiles overlapping each other. We refrain from writing them and simply assume that the four angles are fixed appropriately.

By means of the seven parameters, we can find the coordinates of the vertices:

$$E = (0,0), \quad F = c(\cos\beta, \sin\beta), \quad A = F - (a,0),$$
$$D = -b(\cos\alpha, \sin\alpha), \quad C = D - (a,0),$$

Downloaded from https://royalsocietypublishing.org/ on 27 February 2024

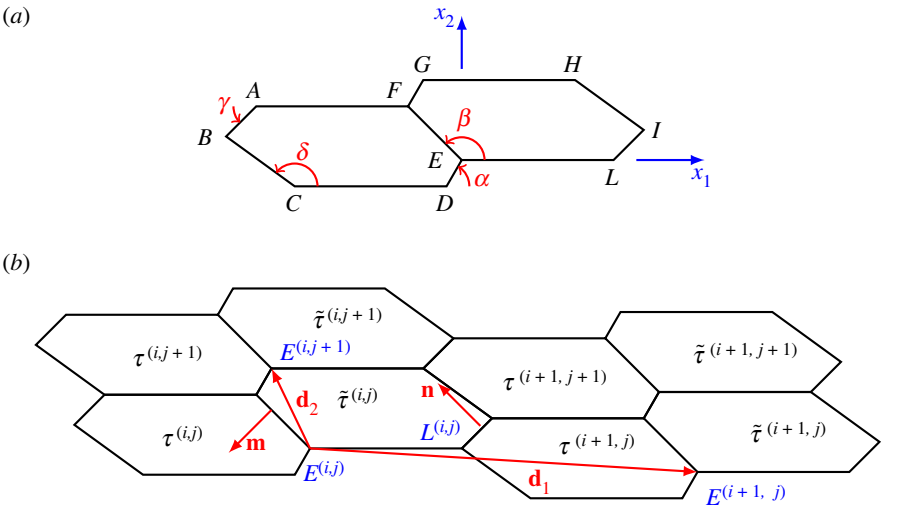

Figure 3. Unit cell and general tessellation, Type 1. (*a*) Geometry of the Type 1 unit cell and (*b*) Type 1 tessellation.

while to determine the coordinates of B we solve the two equations

$$A - t(\cos\gamma, \sin\gamma) = C + s(\cos\delta, \sin\delta).$$

Denoting by $t_\circ$ and $s_\circ$ the solutions of these equations we have that

$$B = A - t_\circ(\cos\gamma, \sin\gamma).$$

Also,

$$G = F + b(\cos\alpha, \sin\alpha), \quad H = G + (a, 0)$$

and

$$L = E + (a, 0), \quad I = L + t_\circ(\cos\gamma, \sin\gamma).$$

The hexagonal region whose vertices are A, B, C, D, E and F will be denoted by τ, while the region delimited by the vertices E, F, G, H, I and L will be denoted by $\tilde{\tau}$. We shall refer to $\tau \cup \tilde{\tau}$ as the unit cell. By means of the vectors

$$\mathbf{d}_1 = L - B = \left(2a - c\,\cos\beta - \frac{\cos\gamma\,(b\,\sin(\alpha-\delta) + c\,\sin(\beta-\delta))}{\sin(\delta-\gamma)}\right)\mathbf{e}_1 - \left(c\,\sin\beta + \frac{\sin\gamma\,(b\,\sin(\alpha-\delta) + c\,\sin(\beta-\delta))}{\sin(\delta-\gamma)}\right)\mathbf{e}_2$$

and

$$\mathbf{d}_2 = G - E = (b\,\cos\alpha + c\,\cos\beta)\mathbf{e}_1 + (b\,\sin\alpha + c\,\sin\beta)\mathbf{e}_2,$$

we generate a tessellation of $\mathbb{R}^3_0$ (figure 3*b*). In particular, for $i, j \in \mathbb{Z}$, we denote by

$$\tau^{(i,j)} = i\mathbf{d}_1 + j\mathbf{d}_2 + \tau = \{i\mathbf{d}_1 + j\mathbf{d}_2 + \mathbf{x} : \mathbf{x} \in \tau\}$$

and

$$\tilde{\tau}^{(i,j)} = i\mathbf{d}_1 + j\mathbf{d}_2 + \tilde{\tau} = \{i\mathbf{d}_1 + j\mathbf{d}_2 + \mathbf{x} : \mathbf{x} \in \tilde{\tau}\},$$

and similarly we denote the translated vertices, for instance, we set

$$E^{(i,j)} = i\mathbf{d}_1 + j\mathbf{d}_2 + E.$$

Let φ be the relative rotation between tiles occupying the regions $\tau^{(i,j)}$ and $\tilde{\tau}^{(i,j)}$, and let $\mathbf{m} = -\sin\beta\,\mathbf{e}_1 + \cos\beta\,\mathbf{e}_2$ be the normal to the segments EF outward to $\tilde{\tau}$ and inward to τ. Similarly,

Downloaded from https://royalsocietypublishing.org/ on 27 February 2024

let ϑ and ψ be the relative rotations 'around' the segment EL and LI, respectively, and let $\mathbf{n} - \sin\gamma\,\mathbf{e}_1 + \cos\gamma\,\mathbf{e}_2$ be the inward normal $\tilde{\tau}^{(i,j)}$ and outward to $\tau^{(i+1,j)}$.

By means of $(2.3)_1$ and $(2.3)_2$, we find

$$\psi = \varphi\frac{\sin\delta\,\sin(\beta-\alpha)}{\sin\alpha\,\sin(\delta-\gamma)} \quad \text{and} \quad \vartheta = \varphi\frac{\sin(\beta-\alpha)}{\sin\alpha}.$$

Denoting by $\mathbf{W}^{(i,j)}$ and $\widetilde{\mathbf{W}}^{(i,j)}$ the infinitesimal rotation tensors of the tiles occupying the regions $\tau^{(i,j)}$ and $\tilde{\tau}^{(i,j)}$, respectively, and applying (2.2) three times, we find

$$\left.\begin{aligned}\widetilde{\mathbf{W}}^{(i,j)} &= \mathbf{W}^{(i,j)} + \varphi\,\mathbf{e}_3\otimes\mathbf{m},\\ \mathbf{W}^{(i,j+1)} &= \mathbf{W}^{(i,j)} - \vartheta\,\mathbf{e}_3\otimes\mathbf{e}_2\\ \text{and}\qquad \mathbf{W}^{(i+1,j)} &= \widetilde{\mathbf{W}}^{(i,j)} + \psi\,\mathbf{e}_3\otimes\mathbf{n}.\end{aligned}\right\} \tag{3.1}$$

For $j=0$, from the first and the third of these identities, we deduce that

$$\mathbf{W}^{(i+1,0)} = \mathbf{W}^{(i,0)} + \mathbf{e}_3\otimes(\varphi\mathbf{m} + \psi\mathbf{n}),$$

and iterating this identity we find that

$$\mathbf{W}^{(i,0)} = \mathbf{W}^{(0,0)} + \mathbf{e}_3\otimes(i\varphi\mathbf{m} + i\psi\mathbf{n}). \tag{3.2}$$

To avoid rigid motions we set $\mathbf{u}(\mathbf{x}) = \mathbf{0}$ for all $\mathbf{x}\in\tau^{(0,0)}$, thus, in particular, $\mathbf{W}^{(0,0)} = \mathbf{0}$. Successively applying the second of (3.1) and (3.2) we find

$$\mathbf{W}^{(i,j)} = \mathbf{e}_3\otimes(i\varphi\mathbf{m} + i\psi\mathbf{n} - j\vartheta\,\mathbf{e}_2),$$

and from the first of (3.1) we deduce that

$$\widetilde{\mathbf{W}}^{(i,j)} = \mathbf{e}_3\otimes((i+1)\varphi\mathbf{m} + i\psi\mathbf{n} - j\vartheta\,\mathbf{e}_2). \tag{3.3}$$

By applying (2.1), we have that

$$\left.\begin{aligned}\mathbf{u}(E^{(i,j+1)}) &= \mathbf{u}(E^{(i,j)}) + \widetilde{\mathbf{W}}^{(i,j)}\mathbf{d}_2,\\ \mathbf{u}(L^{(i,j)}) &= \mathbf{u}(E^{(i,j)}) + a\widetilde{\mathbf{W}}^{(i,j)}\mathbf{e}_1\\ \text{and}\qquad \mathbf{u}(E^{(i+1,j)}) &= \mathbf{u}(L^{(i,j)}) + \mathbf{W}^{(i+1,j)}\mathbf{p},\end{aligned}\right\} \tag{3.4}$$

where we set

$$\mathbf{p} = E - B.$$

By successively applying the first of (3.4), we find

$$\mathbf{u}(E^{(i,j)}) = \mathbf{u}(E^{(i,0)}) + \sum_{k=0}^{j-1}\widetilde{\mathbf{W}}^{(i,k)}\mathbf{d}_2, \tag{3.5}$$

and for $j=0$, from the second and third of (3.4) and the third of (3.1) we deduce that

$$\begin{aligned}\mathbf{u}(E^{(i,0)}) &= \mathbf{u}(L^{(i-1,0)}) + \mathbf{W}^{(i,0)}\mathbf{p}\\ &= \mathbf{u}(E^{(i-1,0)}) + a\widetilde{\mathbf{W}}^{(i-1,0)}\mathbf{e}_1 + \mathbf{W}^{(i,0)}\mathbf{p}\\ &= \mathbf{u}(E^{(i-1,0)}) + a\widetilde{\mathbf{W}}^{(i-1,0)}\mathbf{e}_1 + \widetilde{\mathbf{W}}^{(i-1,0)}\mathbf{p} + \psi\,\mathbf{n}\cdot\mathbf{p}\,\mathbf{e}_3\\ &= \mathbf{u}(E^{(i-1,0)}) + \widetilde{\mathbf{W}}^{(i-1,0)}\mathbf{d}_1 + \psi\,\mathbf{n}\cdot\mathbf{p}\,\mathbf{e}_3,\end{aligned}$$

since $\mathbf{d}_1 = a\mathbf{e}_1 + \mathbf{p}$. Iterating this equation we find

$$\mathbf{u}(E^{(i,0)}) = \mathbf{u}(E^{(0,0)}) + \sum_{k=0}^{i-1}\widetilde{\mathbf{W}}^{(k,0)}\mathbf{d}_1 + i\psi\,\mathbf{n}\cdot\mathbf{p}\,\mathbf{e}_3,$$

Downloaded from https://royalsocietypublishing.org/ on 27 February 2024

and combining this equation with (3.5) we arrive at

$$\mathbf{u}(E^{(i,j)}) = \sum_{k=0}^{i-1} \widetilde{\mathbf{W}}^{(k,0)} \mathbf{d}_1 + \sum_{k=0}^{j-1} \widetilde{\mathbf{W}}^{(i,k)} \mathbf{d}_2 + i\psi \mathbf{n} \cdot \mathbf{p}\, \mathbf{e}_3,$$

since $\mathbf{u}(E^{(0,0)}) = \mathbf{0}$. By making use of (3.3), we find

$$\begin{aligned}\mathbf{u}(E^{(i,j)}) &= \sum_{k=0}^{i-1} \mathbf{e}_3 \otimes ((k+1)\varphi \mathbf{m} + k\psi \mathbf{n})\mathbf{d}_1 + \sum_{k=0}^{j-1} \mathbf{e}_3 \otimes ((i+1)\varphi \mathbf{m} + i\psi \mathbf{n} - k\vartheta \mathbf{e}_2)\mathbf{d}_2 + i\psi \mathbf{n} \cdot \mathbf{p}\, \mathbf{e}_3 \\ &= \mathbf{e}_3 \otimes \left(\frac{(i+1)i}{2} \varphi \mathbf{m} + \frac{(i-1)i}{2} \psi \mathbf{n} \right) \mathbf{d}_1 \\ &\quad + \mathbf{e}_3 \otimes \left((i+1)j\varphi \mathbf{m} + ij\psi \mathbf{n} - \frac{(j-1)j}{2} \vartheta \mathbf{e}_2 \right) \mathbf{d}_2 + i\psi \mathbf{n} \cdot \mathbf{p}\, \mathbf{e}_3.\end{aligned}$$

Let $w(E^{(i,j)}) = \mathbf{u}(E^{(i,j)}) \cdot \mathbf{e}_3$. Then

$$\begin{aligned}w(E^{(i,j)}) &= \left(\frac{(i+1)i}{2} \varphi \mathbf{m} + \frac{(i-1)i}{2} \psi \mathbf{n} \right) \cdot \mathbf{d}_1 \\ &\quad + \left((i+1)j\varphi \mathbf{m} + ij\psi \mathbf{n} - \frac{(j-1)j}{2} \vartheta \mathbf{e}_2 \right) \cdot \mathbf{d}_2 + i\psi \mathbf{n} \cdot \mathbf{p}. \end{aligned} \tag{3.6}$$

For every $i, j \in \mathbb{Z}$, (3.6) allows to evaluate the vertical displacement of the vertex $E^{(i,j)}$.

Equation (3.6) prescribes the displacement on the vertices $E^{(i,j)} = i\mathbf{d}_1 + j\mathbf{d}_2 \subset \mathbb{R}^3_0$, for $i, j \in \mathbb{Z}$. Here we extend the function w to $\mathbb{R}^3_0$, that is we define $w_0 : \mathbb{R}^3_0 \to \mathbb{R}$ such that $w_0(E^{(i,j)}) = w(E^{(i,j)})$ for every $i, j \in \mathbb{Z}$. To define w_0 it suffices to take $i, j \in \mathbb{R}$ and to write the correspondence between i, j and x_1, x_2. Since a generic point $\mathbf{x} \in \mathbb{R}^3_0$ can be written as

$$\mathbf{x} = x_1 \mathbf{e}_1 + x_2 \mathbf{e}_2 = i\mathbf{d}_1 + j\mathbf{d}_2,$$

we have that

$$i = \mathbf{x} \cdot \mathbf{d}^1 \quad \text{and} \quad j = \mathbf{x} \cdot \mathbf{d}^2,$$

where the contravariant vectors $\mathbf{d}^1$ and $\mathbf{d}^2$ are such that $\mathbf{d}^\alpha \cdot \mathbf{d}_\beta = \delta_{\alpha\beta}$. By substituting these identities in (3.6) we find the extension

$$w_0(\mathbf{x}) = \frac{1}{2} \mathbf{K}\mathbf{x} \cdot \mathbf{x} + \mathbf{v} \cdot \mathbf{x}, \tag{3.7}$$

where

$$\mathbf{K} = (\varphi \mathbf{m} + \psi \mathbf{n}) \cdot \mathbf{d}_1\, \mathbf{d}^1 \otimes \mathbf{d}^1 - \vartheta\, \mathbf{e}_2 \cdot \mathbf{d}_2\, \mathbf{d}^2 \otimes \mathbf{d}^2 + (\varphi \mathbf{m} + \psi \mathbf{n}) \cdot \mathbf{d}_2\, (\mathbf{d}^1 \otimes \mathbf{d}^2 + \mathbf{d}^2 \otimes \mathbf{d}^1),$$

and

$$\mathbf{v} = \frac{1}{2} [(\varphi \mathbf{m} + \psi \mathbf{n}) \cdot \mathbf{d}_1 + \psi \mathbf{n} \cdot \mathbf{p}]\, \mathbf{d}^1 + \frac{1}{2} [(\varphi \mathbf{m} + \psi \mathbf{n} - \vartheta \mathbf{e}_2) \cdot \mathbf{d}_2]\, \mathbf{d}^2.$$

Therefore, the metasurface generated with Type 1 tessellations takes the shape of a quadric.

(b) Type 2

To describe the configurations of Type 2, we need six parameters. We take the three angles, α, β and γ, as depicted in figure 4*a*, and three lengths

$$EF = CQ = a, \quad FR = b, \; QR = DE = c.$$

The regions occupied by the four tiles are denoted by $\tau, \tilde{\tau}, \hat{\tau}$ and $\bar{\tau}$, as depicted in the figure.

Let φ be the relative rotation between tiles occupying the regions $\tau^{(i,j)}$ and $\hat{\tau}^{(i,j)}$ and let $\mathbf{m}$ be the normal to the segments QR outward to $\hat{\tau}$ and inward to τ. Similarly, let ϑ, ψ and η be the relative

Downloaded from https://royalsocietypublishing.org/ on 27 February 2024

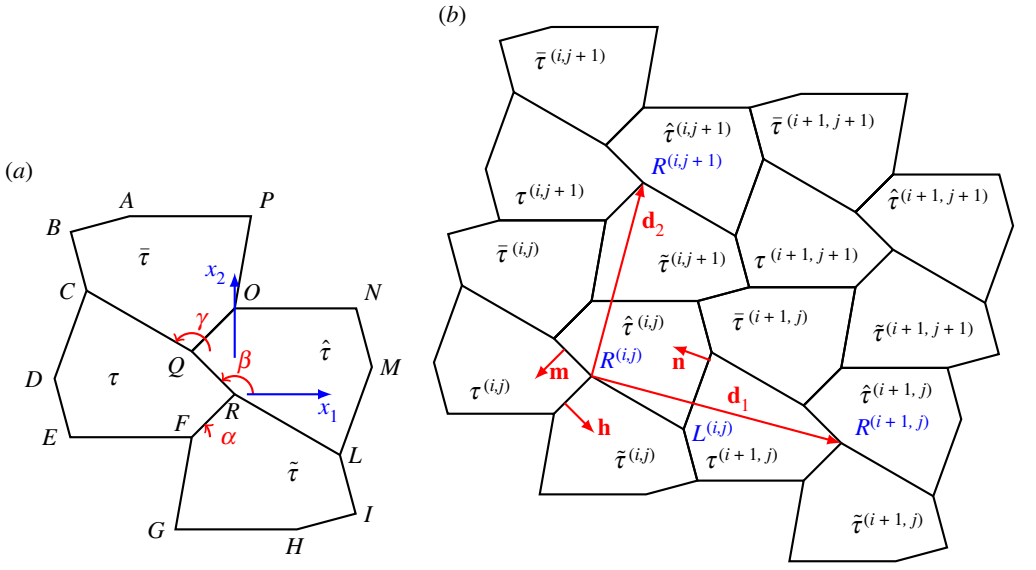

Figure 4. Unit cell and general tessellation, Type 2. (*a*) Geometry of the Type 2 unit cell and (*b*) Type 2 tessellation.

rotations 'around' the segment *LM*, *ON* and *FR*, respectively, and let $\mathbf{h}$ be the normal inward to $\tilde{\tau}^{(i,j)}$ and outward to $\tau^{(i,j)}$, and $\mathbf{n}$ be the normal inward to $\hat{\tau}^{(i,j)}$ and outward to $\tau^{(i+1,j)}$ (figure 4*b*).

$$\left.\begin{aligned}\widehat{\mathbf{W}}^{(i,j)} &= \mathbf{W}^{(i,j)} + \varphi \mathbf{e}_3 \otimes \mathbf{m},\\ \mathbf{W}^{(i,j)} &= \widetilde{\mathbf{W}}^{(i,j)} + \eta \mathbf{e}_3 \otimes \mathbf{h},\\ \widetilde{\mathbf{W}}^{(i,j+1)} &= \widehat{\mathbf{W}}^{(i,j)} - \vartheta \mathbf{e}_3 \otimes \mathbf{e}_2\end{aligned}\right\}$$

and

$$\mathbf{W}^{(i+1,j)} = \widehat{\mathbf{W}}^{(i,j)} + \psi \mathbf{e}_3 \otimes \mathbf{n}.$$

From these equations, we deduce that

$$\mathbf{W}^{(i,j)} = \mathbf{W}^{(0,0)} + \mathbf{e}_3 \otimes \big((i+j)\varphi \mathbf{m} + j\eta \mathbf{h} - j\vartheta \mathbf{e}_2 + i\psi \mathbf{n}\big). \tag{3.8}$$

Let us define the vectors $\mathbf{p}_1 = R - G$, $\mathbf{p}_2 = R - D$. We have that

$$\begin{aligned}\mathbf{u}(R^{(i,j+1)}) &= \mathbf{u}(R^{(i,j)}) + \widehat{\mathbf{W}}^{(i,j)}[O - R] + \widetilde{\mathbf{W}}^{(i,j+1)}\mathbf{p}_1\\ &= \mathbf{u}(R^{(i,j)}) + \mathbf{W}^{(i,j)}\mathbf{d}_2 + \big(\varphi \mathbf{m}\cdot\mathbf{d}_2 - \vartheta \mathbf{e}_2\cdot\mathbf{p}_1\big)\mathbf{e}_3,\end{aligned}$$

and

$$\begin{aligned}\mathbf{u}(R^{(i+1,j)}) &= \mathbf{u}(R^{(i,j)}) + \widehat{\mathbf{W}}^{(i,j)}[L - R] + \mathbf{W}^{(i+1,j)}\mathbf{p}_2\\ &= \mathbf{u}(R^{(i,j)}) + \mathbf{W}^{(i,j)}\mathbf{d}_1 + \big(\varphi \mathbf{m}\cdot\mathbf{d}_1 + \psi \mathbf{n}\cdot\mathbf{p}_2\big)\mathbf{e}_3,\end{aligned}$$

from which it follows that

$$\mathbf{u}(R^{(i,j)}) = \mathbf{u}(R^{(0,0)}) + \sum_{k=0}^{i-1}\big(\mathbf{W}^{(k,0)}\mathbf{d}_1 + \mathbf{W}^{(i,k)}\mathbf{d}_2\big) + i\big(\varphi \mathbf{m}\cdot\mathbf{d}_1 + \psi \mathbf{n}\cdot\mathbf{p}_2\big)\mathbf{e}_3 + j\big(\varphi \mathbf{m}\cdot\mathbf{d}_2 - \vartheta \mathbf{e}_2\cdot\mathbf{p}_1\big)\mathbf{e}_3.$$

Downloaded from https://royalsocietypublishing.org/ on 27 February 2024

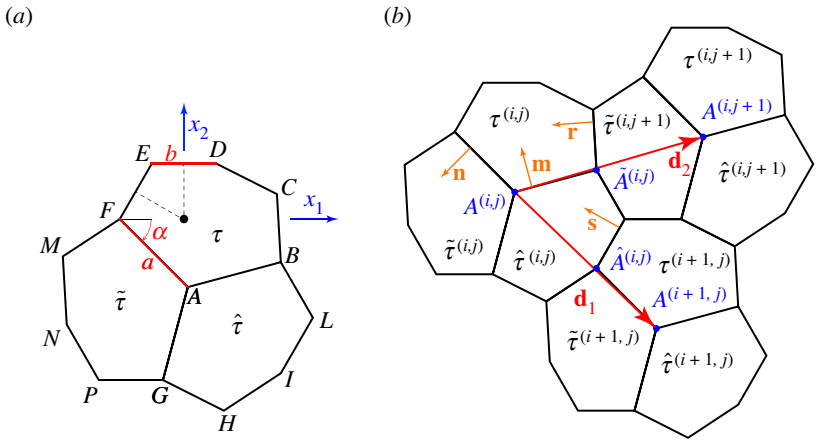

Figure 5. Unit cell and general tessellation, Type 3. (*a*) Geometry of the Type 3 unit cell and (*b*) Type 3 tessellation.

Assuming that $\mathbf{u}(R^{(0,0)}) = \mathbf{0}$ and $\mathbf{W}^{(0,0)} = \mathbf{0}$, and by using (3.8), we finally deduce that

$$\begin{aligned} w(R^{(i,j)}) = {} & \frac{i(i-1)}{2}(\varphi\mathbf{m} + \psi\mathbf{n}) \cdot \mathbf{d}_1 + ij(\varphi\mathbf{m} + \psi\mathbf{n}) \cdot \mathbf{d}_2 \\ & + \frac{j(j-1)}{2}(\varphi\mathbf{m} + \eta\mathbf{h} - \vartheta\mathbf{e}_2) \cdot \mathbf{d}_2 + i(\varphi\mathbf{m} \cdot \mathbf{d}_1 + \psi\mathbf{n} \cdot \mathbf{p}_2) \\ & + j(\varphi\mathbf{m} \cdot \mathbf{d}_2 - \vartheta\mathbf{e}_2 \cdot \mathbf{p}_1). \end{aligned}$$

Finally, we determine the continuous interpolant, which has the same expression as (3.7), with

$$\begin{aligned} \mathbf{K} = {} & (\varphi\mathbf{m} + \psi\mathbf{n}) \cdot \mathbf{d}_1\, \mathbf{d}^1 \otimes \mathbf{d}^1 + (\varphi\mathbf{m} + \eta\mathbf{h} - \vartheta\mathbf{e}_2) \cdot \mathbf{d}_2\, \mathbf{d}^2 \otimes \mathbf{d}^2 \\ & + (\varphi\mathbf{m} + \psi\mathbf{n}) \cdot \mathbf{d}_2(\mathbf{d}^1 \otimes \mathbf{d}^2 + \mathbf{d}^2 \otimes \mathbf{d}^1), \end{aligned}$$

and

$$\mathbf{v} = \left[\frac{1}{2}(\varphi\mathbf{m} - \psi\mathbf{n}) \cdot \mathbf{d}_1 + \psi\mathbf{n} \cdot \mathbf{p}_2\right] \mathbf{d}^1 + \left[\frac{1}{2}(\varphi\mathbf{m} - \eta\mathbf{h} + \vartheta\mathbf{e}_2) \cdot \mathbf{d}_2 - \vartheta\mathbf{e}_2 \cdot \mathbf{p}_1\right] \mathbf{d}^2.$$

Therefore, the metasurface generated with Type 2 tessellation is again a quadric. The explicit formulae relating the contravariant vectors $\mathbf{d}^1$, $\mathbf{d}^2$, the angles φ, ψ, ϑ, and the vectors $\mathbf{m}$, $\mathbf{n}$, $\mathbf{h}$ to the six geometric parameters are quite convoluted and involved. For brevity and clarity, we choose to omit them in this context.

(c) Type 3

To describe the configuration of Type 3, we need three parameters. We choose the two lengths a and b and the angle α represented in figure 5.

The hexagonal region whose vertices are A, B, C, D, E and F will be denoted by τ, while the region delimited by the vertices $AGHLI$, and B will be denoted by $\hat{\tau}$; the third region, delimited by $AFMNP$, and G, will be denoted by $\tilde{\tau}$. We shall refer to $\tau \cup \hat{\tau} \cup \tilde{\tau}$ as unit cell. By means of the vectors

$$\mathbf{d}_1 = L - E \quad \text{and} \quad \mathbf{d}_2 = C - M,$$

we generate a tessellation of $\mathbb{R}^3_0$. We also introduce the vectors $\mathbf{p}_1 = I - A, \mathbf{p}_2 = B - A$, and the translated vertices

$$A^{(i,j)} = i\mathbf{d}_1 + j\mathbf{d}_2 + A, \quad \widehat{A}^{(i,j)} = A^{(i,j)} + \mathbf{p}_1, \ \widetilde{A}^{(i,j)} = A^{(i,j)} + \mathbf{p}_2.$$

Let φ be the relative rotation between the tiles occupying the regions $\tau^{(i,j)}$ and $\tilde{\tau}^{(i,j)}$ and let $\mathbf{n}$ be the normal to the segment AF outward to τ and inward to $\tilde{\tau}$. Since the three segments emanating

Downloaded from https://royalsocietypublishing.org/ on 27 February 2024

from A form an angle of $2/3\pi$ with each other, the relative rotations between the three tiles τ, $\tilde{\tau}$ and $\hat{\tau}$ are the same. Moreover, let $\mathbf{r}$ denote the normal vector outward to $\tilde{\tau}^{(i,j+1)}$ and inward to $\tau^{(i,j)}$, while let ψ be the relative rotation; analogously, let $\mathbf{s}$ denote the normal vector outward to $\tau^{(i+1,j)}$ and inward to $\hat{\tau}^{(i,j)}$, while let ϑ be the relative rotation. Denoting by $\mathbf{W}^{(i,j)}$, $\widetilde{\mathbf{W}}^{(i,j)}$ and $\widehat{\mathbf{W}}^{(i,j)}$ the infinitesimal rotation tensors of the tiles occupying the regions $\tau^{(i,j)}$, $\tilde{\tau}^{(i,j)}$ and $\hat{\tau}^{(i,j)}$, respectively, and applying (2.2), we find:

$$\left.\begin{aligned}
&\widetilde{\mathbf{W}}^{(i,j)} = \mathbf{W}^{(i,j)} - \varphi\, \mathbf{e}_3 \otimes \mathbf{n},\\
&\widehat{\mathbf{W}}^{(i,j)} = \mathbf{W}^{(i,j)} + \varphi\, \mathbf{e}_3 \otimes \mathbf{m},\\
&\widetilde{\mathbf{W}}^{(i,j+1)} = \mathbf{W}^{(i,j)} + \psi\, \mathbf{e}_3 \otimes \mathbf{r},\\
&\mathbf{W}^{(i+1,j)} = \widehat{\mathbf{W}}^{(i,j)} + \vartheta\, \mathbf{e}_3 \otimes \mathbf{s} = \mathbf{W}^{(i,j)} + \mathbf{e}_3 \otimes (\varphi\, \mathbf{m} + \vartheta\, \mathbf{s})\\
\text{and}\quad &\mathbf{W}^{(i,j+1)} = \widetilde{\mathbf{W}}^{(i,j+1)} + \varphi\, \mathbf{e}_3 \otimes \mathbf{n} = \mathbf{W}^{(i,j)} + \mathbf{e}_3 \otimes (\psi\, \mathbf{r} + \varphi\, \mathbf{n}).
\end{aligned}\right\} \tag{3.9}$$

For $j = 0$, from $(3.9)_4$, we deduce

$$\mathbf{W}^{(i+1,0)} = \mathbf{W}^{(i,0)} + \mathbf{e}_3 \otimes (\varphi\, \mathbf{m} + \vartheta\, \mathbf{s}),$$

and iterating, we find:

$$\mathbf{W}^{(i,0)} = \mathbf{e}_3 \otimes (i\varphi\, \mathbf{m} + i\vartheta\, \mathbf{s}),$$

where we have set $\mathbf{W}^{(0,0)} = \mathbf{0}$ to avoid rigid motions. From $(3.9)_5$, we then find

$$\mathbf{W}^{(i,j)} = \mathbf{e}_3 \otimes (i\varphi\, \mathbf{m} + i\vartheta\, \mathbf{s} + j\psi\, \mathbf{r} + j\varphi\, \mathbf{n}).$$

Finally, from $(3.9)_{1,2}$ we get

$$\left.\begin{aligned}
&\widetilde{\mathbf{W}}^{(i,j)} = \mathbf{e}_3 \otimes (i\varphi\, \mathbf{m} + i\vartheta\, \mathbf{s} + j\psi\, \mathbf{r} + (j-1)\varphi\, \mathbf{n})\\
\text{and}\quad &\widehat{\mathbf{W}}^{(i,j)} = \mathbf{e}_3 \otimes ((i+1)\varphi\, \mathbf{m} + i\vartheta\, \mathbf{s} + j\psi\, \mathbf{r} + j\varphi\, \mathbf{n}).
\end{aligned}\right\} \tag{3.10}$$

By applying (2.1) we have that

$$\left.\begin{aligned}
&\mathbf{u}(\widehat{A}^{(i,j)}) = \mathbf{u}(A^{(i,j)}) + \widehat{\mathbf{W}}^{(i,j)}\mathbf{p}_1,\\
&\mathbf{u}(\widetilde{A}^{(i,j)}) = \mathbf{u}(A^{(i,j)}) + \mathbf{W}^{(i,j)}\mathbf{p}_2,\\
&\mathbf{u}(A^{(i+1,j)}) = \mathbf{u}(\widehat{A}^{(i,j)}) + \mathbf{W}^{(i+1,j)}(\mathbf{d}_1 - \mathbf{p}_1) = \mathbf{u}(A^{(i,j)}) + \widehat{\mathbf{W}}^{(i,j)}\mathbf{p}_1 + \mathbf{W}^{(i+1,i)}(\mathbf{d}_1 - \mathbf{p}_1)\\
\text{and}\quad &\mathbf{u}(A^{(i,j+1)}) = \mathbf{u}(\widetilde{A}^{(i,j)}) + \widetilde{\mathbf{W}}^{(i,j+1)}(\mathbf{d}_2 - \mathbf{p}_2) = \mathbf{u}(A^{(i,j)}) + \mathbf{W}^{(i,j)}\mathbf{p}_2 + \widetilde{\mathbf{W}}^{(i,j+1)}(\mathbf{d}_2 - \mathbf{p}_2).
\end{aligned}\right\}$$

With similar calculations as those already presented, we get

$$\mathbf{u}(A^{(i,j)}) = \sum_{k=1}^{j} \widetilde{\mathbf{W}}^{(i,k)}(\mathbf{d}_2 - \mathbf{p}_2) + \sum_{k=0}^{i-1} \widehat{\mathbf{W}}^{(k,0)}\mathbf{d}_1 + i\vartheta\, \mathbf{s} \cdot (\mathbf{d}_1 - \mathbf{p}_1)\, \mathbf{e}_3 + \sum_{k=0}^{j-1} \mathbf{W}^{(i,k)}\mathbf{p}_2,$$

where we have set $\mathbf{u}(A^{(0,0)}) = \mathbf{0}$. By making use of (3.10), we finally obtain:

$$\begin{aligned}
w(A^{(i,j)}) = &\left(j(i\varphi\mathbf{m} + i\vartheta\mathbf{s}) + \frac{(j+1)j}{2}\psi\mathbf{r} + \frac{(j-1)j}{2}\varphi\mathbf{n}\right) \cdot (\mathbf{d}_2 - \mathbf{p}_2)\\
&+ \left(\frac{(i+1)i}{2}\varphi\mathbf{m} + \frac{i(i-1)}{2}\vartheta\mathbf{s}\right) \cdot \mathbf{d}_1 + i\vartheta\, \mathbf{s} \cdot (\mathbf{d}_1 - \mathbf{p}_1)\\
&+ \left(ij(\varphi\mathbf{m} + \vartheta\mathbf{s}) + \frac{(j-1)j}{2}\psi\mathbf{r} + \frac{(j-1)j}{2}\varphi\mathbf{n}\right) \cdot \mathbf{p}_2.
\end{aligned}$$

Finally, we determine the continuous interpolant, which has the same expression as (3.7), where

$$\mathbf{K} = (\varphi\mathbf{m} + \vartheta\mathbf{s}) \cdot \mathbf{d}_1\, \mathbf{d}^1 \otimes \mathbf{d}^1 + (\psi\mathbf{r} + \varphi\mathbf{n}) \cdot \mathbf{d}_2\, \mathbf{d}^2 \otimes \mathbf{d}^2 + (\varphi\mathbf{m} + \vartheta\mathbf{s}) \cdot \mathbf{d}_2(\mathbf{d}^1 \otimes \mathbf{d}^2 + \mathbf{d}^2 \otimes \mathbf{d}^1) \tag{3.11}$$

Downloaded from https://royalsocietypublishing.org/ on 27 February 2024

and

$$\mathbf{v} = \left[\frac{1}{2}(\varphi\mathbf{m} + \vartheta\mathbf{s})\cdot\mathbf{d}_1 + \vartheta\mathbf{s}\cdot\mathbf{p}_1\right]\mathbf{d}^1 + \left[\frac{1}{2}(\psi\mathbf{r} - \varphi\mathbf{n})\cdot\mathbf{d}_2 - \psi\mathbf{r}\cdot\mathbf{p}_2\right]\mathbf{d}^2. \tag{3.12}$$

Therefore, the metasurface generated with Type 3 tessellation is again a quadric. Remarkably, for $\alpha = \pi$, $\mathbf{K} = \mathbf{0}$, while $\mathbf{v} = \sqrt{3}/2(a+b)\varphi\,\mathbf{d}^2$; therefore, the deformed metasurface turns out to be planar (see fig. 18 (c) of Part I). Furthermore, due to the presence of a threefold symmetry axis in the unit cell, the curvature tensor $\mathbf{K}$ is proportional to the identity, which can be easily observed by expressing (3.11) in Cartesian coordinates. Consequently, the metasurface always exhibits synclastic curvature.

4. Parametric analysis

To comprehend the significance of geometric parameters in programming metasurfaces, this section explores several basic examples. Although these examples do not encompass the entirety of every possible scenario, they offer sufficient representation of the potential benefits of our design approach. Ultimately, this knowledge will enable us to optimize our design methodology, leading to more efficient and effective tessellated plate designs.

We limit ourselves to Type 1 tessellations. Let us denote by $(a_0, b_0, c_0, \alpha_0, \beta_0, \gamma_0, \delta_0)$ the geometric parameters corresponding to the regular hexagon with unitary side, i.e. $a_0 = b_0 = c_0 = 1$, $\alpha_0 = \gamma_0 = \pi/3$, $\beta_0 = \delta_0 = 2/3\pi$.

(a) Role of the sides length

We first consider a family of tiles for which $a = \mathtt{n}a_0$, parametrized by $\mathtt{n} \geq 1$; all the other geometric quantities are those of the regular hexagons. In this case, the tensor $\mathbf{K}$ admits a simple spectral representation:

$$\mathbf{K} = -\frac{\sqrt{3}}{1+2\mathtt{n}}\mathbf{e}_1 \otimes \mathbf{e}_1 - \frac{\sqrt{3}}{3}\mathbf{e}_2 \otimes \mathbf{e}_2. \tag{4.1}$$

Therefore, the principal curvatures are always negative and the principal directions coincide with $\mathbf{e}_1$ and $\mathbf{e}_2$. The curvature in direction $\mathbf{e}_2$ is constant, while that in direction $\mathbf{e}_1$ decreases for $\mathtt{n}$ increasing. The Gaussian curvature turns out to be $1/(1+2\mathtt{n})$; it is therefore always positive and tends to decrease for $\mathtt{n}$ increasing.

For $\mathbf{e}(\phi) = \cos\phi\,\mathbf{e}_1 + \sin\varphi\,\mathbf{e}_2$, $\phi \in [0, 2\pi)$, let us denote by $\kappa(\phi)$ the curvature in direction $\mathbf{e}(\phi)$, *i.e.*, $\kappa(\phi) = \mathbf{K}\mathbf{e}(\phi)\cdot\mathbf{e}(\phi)$. In figure 6*a*, we represent the polar diagram of $\kappa(\phi)$ for various values of $\mathtt{n}$. This makes evident what (4.1) predicts: the circle corresponds to regular hexagons, for which the curvature is the same in every direction; for $\mathtt{n}$ increasing, the hexagon tends to become more and more elongated in direction $\mathbf{e}_1$, which results in a decrease in curvature in the $\mathbf{e}_2$ direction. In figure 6*a*, we also associated to some curves the shape of the deformed configuration and the corresponding tile.

We now consider a family of tiles for which $b = \mathtt{n}b_0$. In this case, the curvature $\mathbf{K}$ admits the following spectral representation:

$$\mathbf{K} = -\frac{\sqrt{3}}{1+2\mathtt{n}}\mathbf{v}_1 \otimes \mathbf{v}_1 - \frac{\sqrt{3}}{3}\mathbf{v}_2 \otimes \mathbf{v}_2, \quad \mathbf{v}_1 = \frac{1}{2}\mathbf{e}_1 + \frac{\sqrt{3}}{2}\mathbf{e}_2,\ \mathbf{v}_2 = -\frac{\sqrt{3}}{2}\mathbf{e}_1 + \frac{1}{2}\mathbf{e}_2. \tag{4.2}$$

For every $\mathtt{n}$, the principal curvatures are in direction $\mathbf{v}_1$ and $\mathbf{v}_2$, being constant the curvature in direction $\mathbf{v}_2$; as in the previous case, the curvature in direction $\mathbf{v}_1$ decreases for $\mathbf{n}$ increases. The Gaussian curvature is always positive. Figure 6*b* reports the polar diagram of the curvature $\kappa(\phi)$, with some deformed configurations and the corresponding tiles.

Downloaded from https://royalsocietypublishing.org/ on 27 February 2024

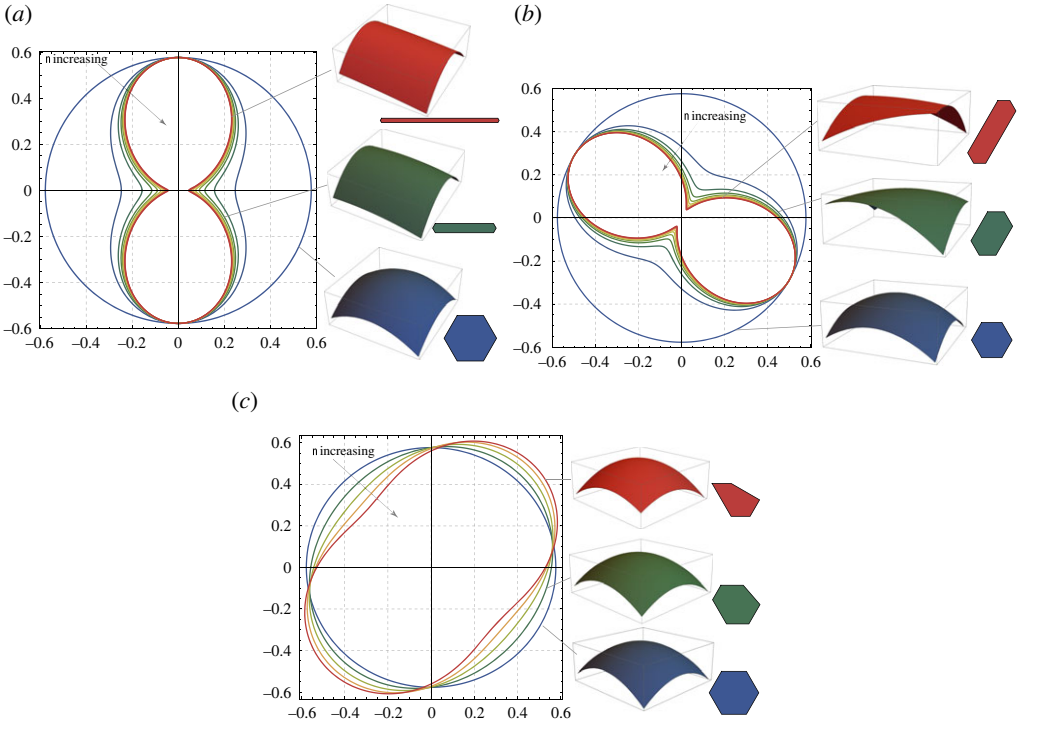

Figure 6. Parametric analysis for Type 1 tessellation, exploring the role of the sides length. (*a*) Polar diagram of the curvature $\kappa(\phi)$ for $a = \mathtt{n}a_0$. (*b*) Polar diagram of the curvature $\kappa(\phi)$ for $b = \mathtt{n}b_0$. (*c*) Polar diagram of the curvature $\kappa(\phi)$ for $c = \mathtt{n}c_0$.

Finally, we consider the case $c = \mathtt{n}c_0$. For this geometry, the spectral representation of $\mathbf{K}$ is quite complicated and we omit it. We notice that both the principal curvatures and the principal directions (slightly) depend on $\mathtt{n}$. In figure 6*c*, we reported the polar diagram of the curvature $\kappa(\phi)$, with some deformed configurations and the corresponding tiles.

(b) Role of the angles

Unlike the previous case, varying the angles can lead to the generation of concave tiles, which ultimately results in surfaces with Gaussian curvature that is not necessarily positive. We first consider a family of tiles for which $\alpha = \mathtt{n}\alpha_0$, $\beta = \beta_0/\mathtt{n}$, while all the other parameters coincide with those of the regular hexagon. In figure 7*a*, it can be observed that, as $\mathtt{n}$ increases, the principal curvature directions are rotated compared with the case of regular tiles, and one of the two principal curvatures tends towards zero. This latter case corresponds to a cylindrical surface with zero Gaussian curvature. If $\mathtt{n}$ continues to increase, then the curvature in the opposite direction begins to grow, while the other curvature decreases, tending towards zero and creating a new cylindrical surface with zero curvature in the direction opposite to the first.

A similar scenario is shown in figure 7*b*. In this case, we have fixed $\alpha = \mathtt{n}\alpha_0$, $\beta = \beta_0/\mathtt{n}$, $\gamma = \mathtt{n}\gamma_0$ and $\delta = \delta_0/\mathtt{n}$. As $\mathtt{n}$ increases, it can be observed that the principal directions rotate slightly. In contrast to the previous case, where both principal curvatures initially decreased, now one of the curvatures tends to increase significantly, while the other decreases. This happens until one of the curvatures becomes zero, producing a cylindrical surface. As $\mathtt{n}$ continues to increase, the previously zero curvature begins to increase again.

(c) The geometric Poisson ratio

By considering the continuum displacement $w_0(\mathbf{x})$, we can introduce the concept of Poisson ratio in relation to bending. The displacement of rectangular elastic, isotropic plate, whose edges are

Downloaded from https://royalsocietypublishing.org/ on 27 February 2024

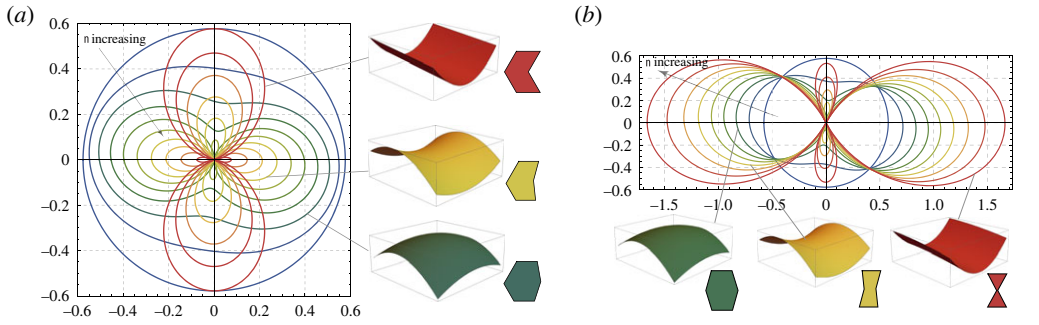

Figure 7. Parametric analysis for Type 1 tessellation, exploring the role of the angles. (*a*) Polar diagram of the curvature $\kappa(\phi)$ for $\alpha = \mathtt{n}\alpha_0$ and $\beta = \beta_0/\mathtt{n}$, (*b*) polar diagram of the curvature $\kappa(\phi)$ for $\alpha = \mathtt{n}\alpha_0$, $\beta = \beta_0/\mathtt{n}$, $\gamma = \mathtt{n}\gamma_0$ and $\delta = \delta_0/\mathtt{n}$.

aligned with the x- and y-axes, can be determined as:

$$w(x,y) = \frac{-M_x}{2\mathcal{D}(1-(\nu^{(b)})^2)}(x^2 - \nu^{(b)}y^2), \tag{4.3}$$

where $\mathcal{D}$ is the bending stiffness, and

$$\nu^{(b)} = -\frac{\partial_{yy}w}{\partial_{xx}w}, \tag{4.4}$$

is the bending Poisson ratio, representing the negative ratio between the transverse curvature and the axial curvature for a uniaxial bending state.

The expression (4.3) holds if the material is elastic, isotropic. Nevertheless, inspired by (4.4) we can define the *geometric Poisson ratio*

$$\varrho = -\frac{K_m}{K_M}, \tag{4.5}$$

where K_m and K_M are the minimum and maximum principal curvatures, respectively. Note that ϱ is a purely geometric quantity and does not have limits.

Let us consider a family of tiles with $a = a_0$, $b = b_0$, $c = c_0$, $\alpha = \mathtt{n}\alpha_0$, $\beta = \beta_0/\mathtt{n}$, $\gamma = \mathtt{m}\gamma_0$, $\delta = \delta_o/\mathtt{m}$), parametrized by the numbers $\mathtt{n} \geq 1$, $\mathtt{m} \geq 1$.

In figure 8, we plotted the values of the coefficient η in terms of $\mathtt{n}$, for several values of fixed $\mathtt{m}$. For $\mathtt{n} = \mathtt{m} = 1$, i.e. for hexagonal tiles, the coefficient turns out to be -1: the surface is synclastic and the two principal curvatures are the same. Varying $\mathtt{n}$ and $\mathtt{m}$ it is possible to obtain a large spectrum of target geometric Poisson ratio, including anticlastic and monoclastic cases.

5. Experimental analysis

In this section, we show the design, manufacturing and experimental testing of physical prototypes of the tessellated metasurfaces with 1 d.f., resulting from the periodic repetition of hexagonal monotiles with three different shapes.

(a) Design of the hexagonal monotiles

We adopt a modular building approach for the assembly of the tessellated plates, using rigid monotiles and flexible connectors. We resort to additive manufacturing technologies, namely fused-deposition modelling (FDM), to three-dimensional print the hexagonal monotiles and the connectors. The rigid monotiles have a side length of 20 mm and are built of two complementary rigid pieces, which can be clamped together, nesting up to six flexible connectors. Once the two pieces are clamped, the connectors become secured and can be linked to adjacent monotiles. The overall thicknesses of the monotiles and connectors is 4.0 and 2.0 mm, respectively. Three

Downloaded from https://royalsocietypublishing.org/ on 27 February 2024

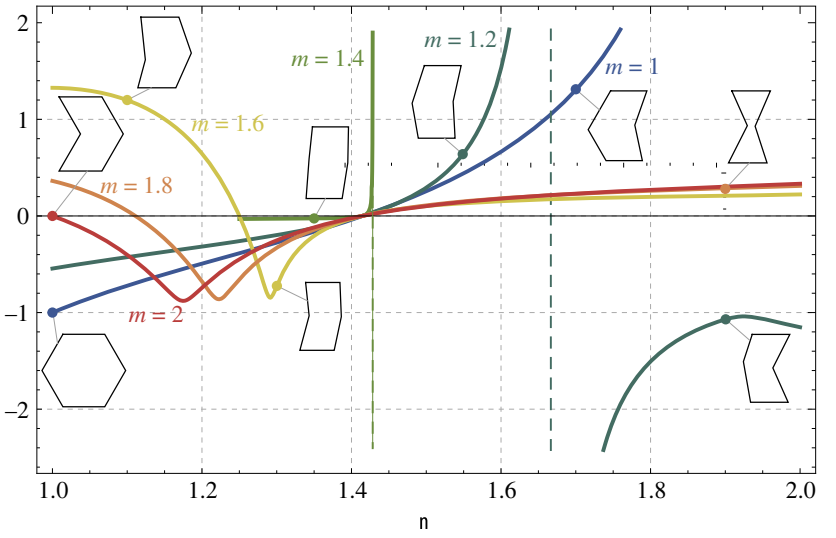

Figure 8. Geometric Poisson ratio ϱ in terms of n, for several fixed values of m.

different types of hexagonal monotiles are considered, in order to obtain synclastic, monoclastic and anticlastic metasurfaces. The flexible connectors are designed to be interchangeable, allowing to connect tiles of different configurations. In figure 9, we show the design drawings of the tiles, connector and tile assembly. The gap between the rigid tiles is limited to 1 mm, providing sufficient clearance to allow for the full development of the rotations along the edges of the tiles. In figure 10*a–c* we show the tessellated metasurfaces assembly principle, for the three types of monotiles considered. One can see that the same universal connector is used for all the hexagonal monotiles. One of the advantages of using universal connectors is that one can use distinct monotiles, within the same tessellated plate combining surfaces with different geometric Poisson ratios.

(b) Manufacturing of the tessellated metasurfaces

The tessellated plates are manufactured resorting to a FDM three-dimensional printer (Original Prusa i3 MK3S). Polyethylene terephthalate glycol (PETg) and polyurethane (Flexfill TPU 92A) filaments are used for the materialization of the rigid monotiles and flexible connectors, respectively. In figure 11 is presented the assembly process of the tessellated plates, using the three different three-dimensional printed hexagonal monotiles with the flexible connectors. In figure 11*a–c* are shown the anticlastic, monoclastic and synclastic cases, respectively. In figure 11*d* is shown an assembly scheme of a tessellated metasurface combining all the different tiles. In this figure, it is also possible to see both the top and bottom pieces of the rigid monotiles, and the positioning of the universal connectors.

(c) Experimental tests

Each tessellated metasurface comprises 37 rigid hexagonal monotiles and 90 flexible connectors. To test the behaviour of the plates when subjected to a given curvature, a curvature enforcer was three-dimensional printed, with a radius of curvature equal to 600 mm, as shown in figure 12. The plates were placed over the curvature enforcer with double-sided mounting tape. The curvature enforcer was positioned along the armchair directions of the tessellated plates, which responded quite reactively to the imposed curvature. In figure 13, one can see the plates subjected to an imposed curvature along the armchair direction with a curvature radius of 600 mm. An Artec3D

Downloaded from https://royalsocietypublishing.org/ on 27 February 2024

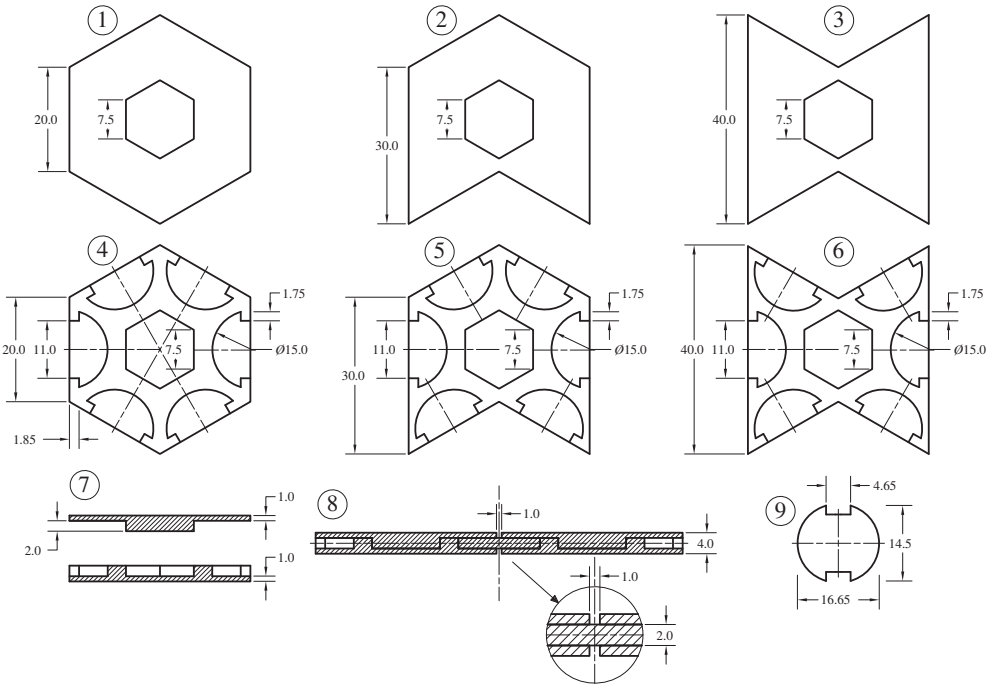

Figure 9. Design drawings: 1 and 4, Convex top and bottom pieces; 2 and 5, Convex - concave top and bottom pieces; 3 and 6, Concave top and bottom pieces; 7, Transversal section along the mid-axis of the tiles; 8, Transversal section along the mid-axis of the tile assembly; 9, Universal connector (all dimensions in mm).

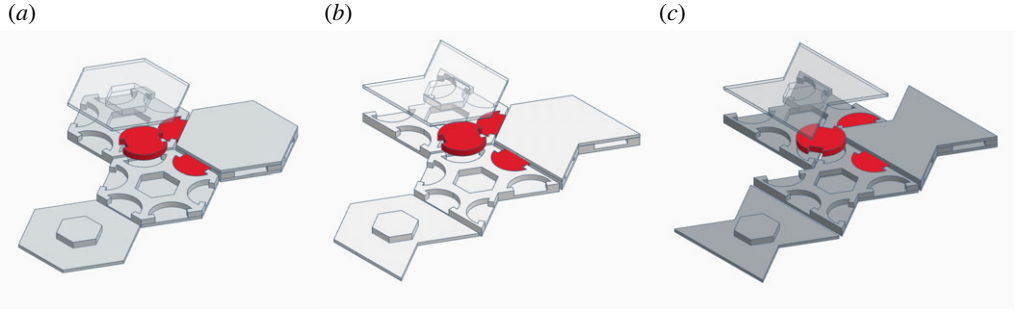

Figure 10. Three-dimensional rendering of the tessellated metasurfaces assembly for different types of hexagonal monotiles. The same universal connector is used for all the monotiles. (*a*) Convex monotile. (*b*) Convex–concave monotile. (*c*) Concave monotile.

Eva scanner was used to build virtual models of the plates, which accurately reflect the physical tessellated metasurfaces with the imposed curvature. In figure 14 are shown two-dimensional images of the digital twins of the tessellated plates, for the synclastic, monoclastic and anticlastic cases. Finally, with the virtual three-dimensional models of the tessellated plates it was possible to identify the curvatures of the plates along the perpendicular direction of the imposed curvatures, as a measure of the quality of the response of the plates. In figure 15 are plotted the configurations of the plates when subjected to the imposed curvature along the armchair direction (input). The output configurations represent the configurations of the plates along the perpendicular direction (zig–zag) (all dimensions in mm).

Downloaded from https://royalsocietypublishing.org/ on 27 February 2024

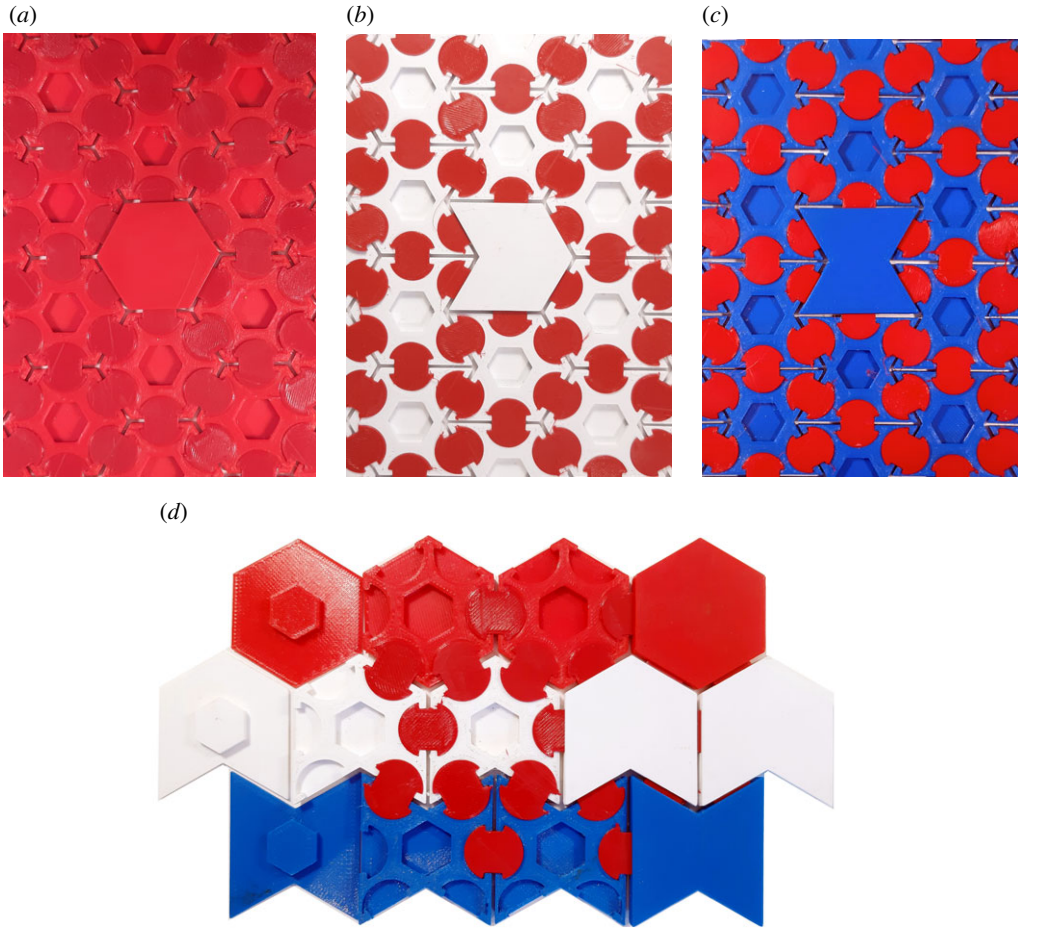

Figure 11. Tessellated metasurfaces assembly with different hexagonal monotiles. (*a*) Anticlastic plate, (*b*) monoclastic plate, (*c*) synclastic plate and (*d*) multi-tiled plate.

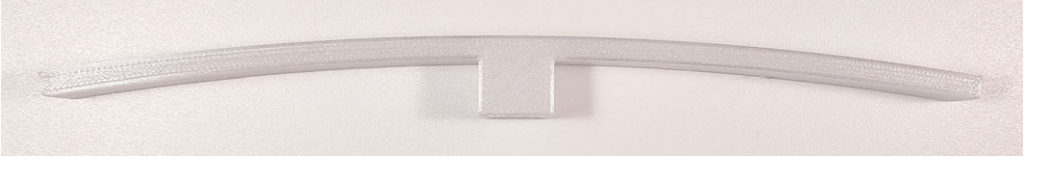

Figure 12. Curvature enforcer for the tessellated metasurfaces ($R = 600$ mm).

One can see in figure 15 that, when subjected to an input curvature with a radius of 600 mm, one obtains an equal output curvature along the perpendicular direction of the synclastic metamaterial plate. This is a clear indicator that the plate behaves according to the analytical results, showing a single mode behaviour. The response of the monoclastic plate shows that one obtains almost zero curvature along the zig–zag direction of the plate, when enforcing a curvature along the armchair direction. Regarding the anticlastic plate, one is able to obtain a tessellated metasurface with negative Gaussian curvature. All the tested plates showed an excellent behaviour, for the imposed curvature, presenting shapes that are consistent with the theoretical results.

Downloaded from https://royalsocietypublishing.org/ on 27 February 2024

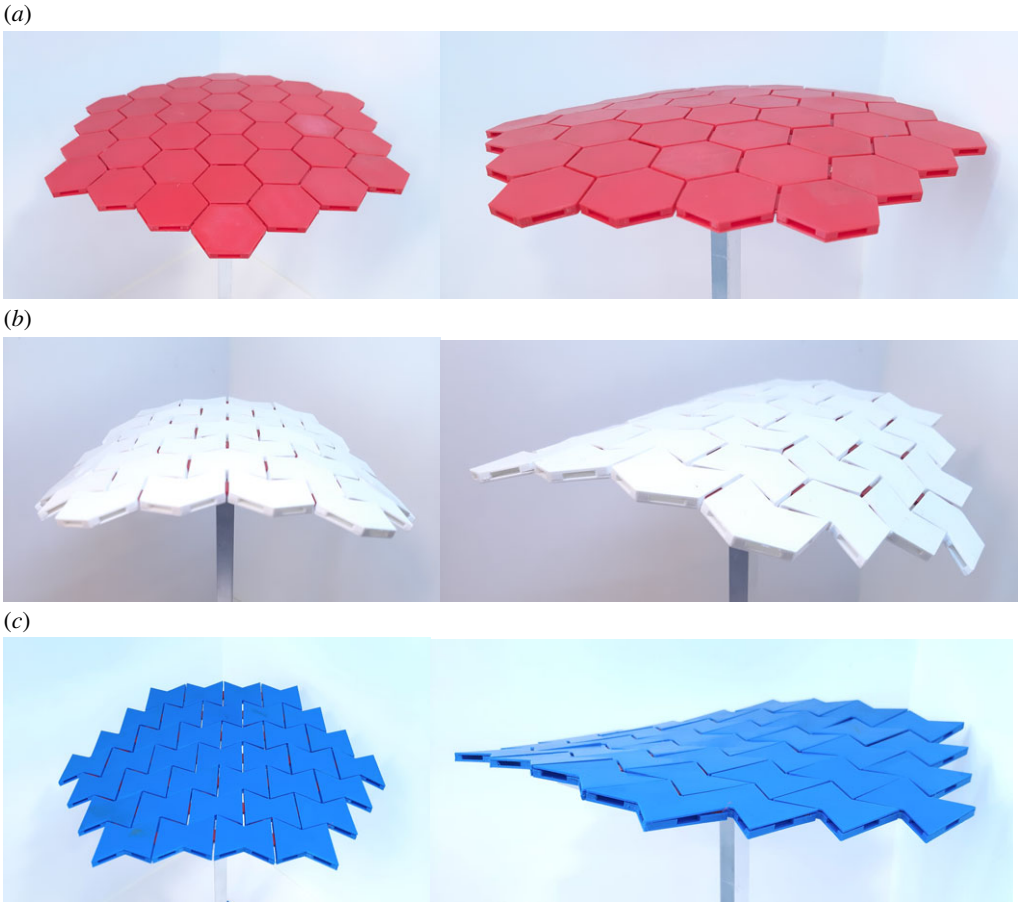

Figure 13. Tessellated plates subjected to an imposed curvature along the armchair direction ($R = 600$ mm). (*a*) Synclastic metamaterial plate, (*b*) monoclastic metamaterial plate, (*c*) anticlastic metamaterial plate.

After the validation of the proposed design scheme for the individual tessellated metasurfaces, we close this section by showing two additional tessellated plates, combining different types of monotiles. In figure 16, we show two models of a large tessellated metasurface with and without the monoclastic transition.

6. Conclusion

This two-part report presented a comprehensive analysis of shape-morphing metasurfaces obtained from infinitesimal origami maps of hexagonal tessellations. The three known types of tessellations composed of congruent irregular hexagons were characterized both at the discrete and continuum level. After showing that Type 1, 2, 3 of tessellated plates possess just one deformation mode (under some conditions for Type 2), we simulated several cases numerically, obtaining metasurfaces with synclastic, anticlastic and monoclastic shapes. In some cases, we observed a marked surface roughness at the level of the repeating unit cell. An essential tool to programme a specified shape consists in the analytical expression of the continuous interpolant of the deformed configuration, which we calculated to be a quadric whose coefficients are expressed in terms of the edge lengths and angles of the monotile. A modular fabrication method was adopted to realize physical models of the proposed tessellated plates, which achieved excellent geometric accuracy with respect to analytical predictions.

Downloaded from https://royalsocietypublishing.org/ on 27 February 2024

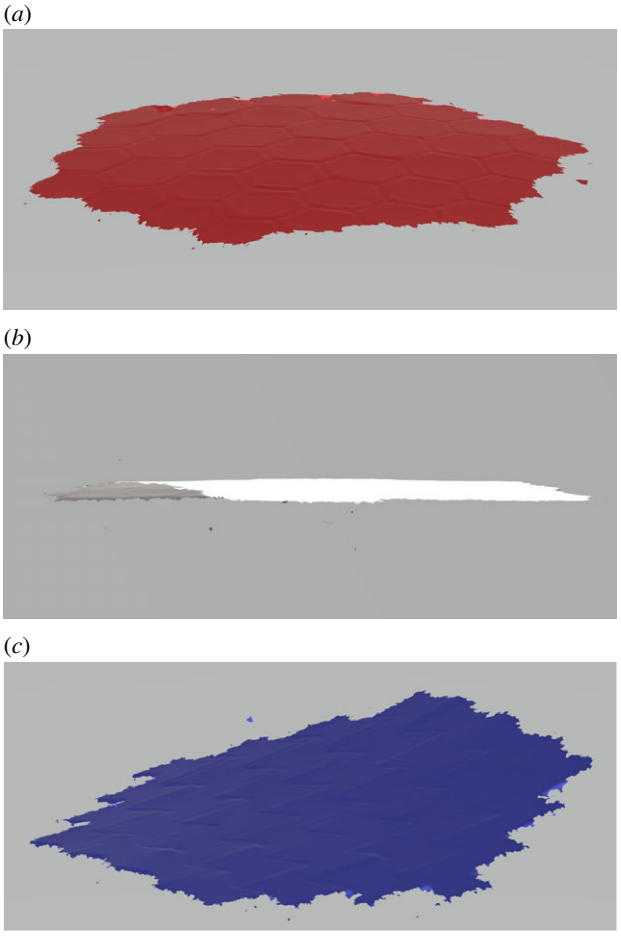

Figure 14. Three-dimensional scanned surfaces of the tessellated metasurfaces. (*a*) Synclastic surface, (*b*) monoclastic surface and (*c*) anticlastic surface.

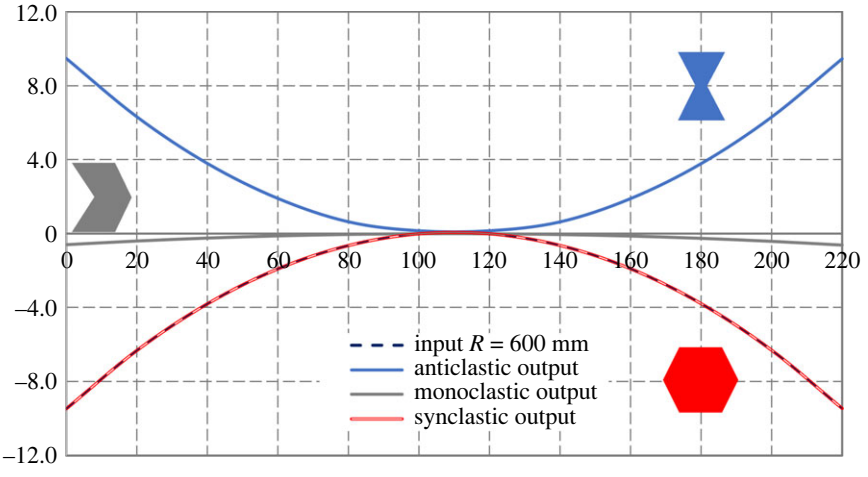

Figure 15. Configurations of the tessellated plates when subjected to imposed curvatures along the armchair direction (input). The output configuration represents the configuration of the plate along the perpendicular direction (zig–zag) (all dimensions in mm).

Downloaded from https://royalsocietypublishing.org/ on 27 February 2024

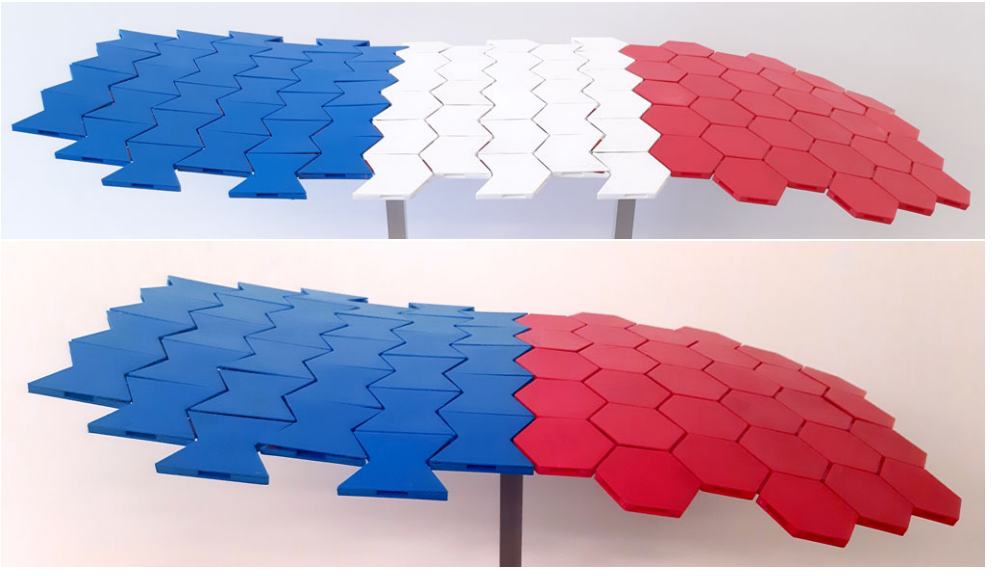

Figure 16. Tessellated metasurface with and without the monoclastic transition.

We envisage practical applications of the proposed metasurfaces in all those areas where geometric accuracy and/or a limited number of actuators are required. For instance, our tessellated plates could be employed: in biomedical engineering to form bone plates [4,5] or patches for tissues and organs [6] that can be customized and adapted to different shapes; as elements of protective armours, exoskeletal systems and wearable devices [7,8] to better conform to different body parts; for components of energy harvesters whose vibration mode is chosen by design [9–11]; as metasurfaces with tunable wettability and friction [12,13] by regulation of the surface roughness; as active architectural facades, tunable-focus mirrors or surfaces of controllable aerodynamic properties [14–17].

Future extensions of this study may regard other monohedral polygonal tessellations, as well as aperiodic and heterogeneous tessellations, to find out the number of deformation modes and the modes shape. In addition, the problem of the inverse design of the tessellations to obtain a target surface may be addressed. Moreover, the performances of plates realized by different fabrication methods could be explored. For instance, tessellated plates could be obtained by laser-cutting regular plates to form lamina torsion joints [18] between adjacent tiles. Another possibility could be given by dual-material additive manufacturing [19], where the stiff and the soft material, for tiles and junctions respectively, can be three-dimensional printed simultaneously. Carving a regular plate along the edges of the tessellation to form flexible hinges could be another alternative using CNC machines. Different fabrication solutions could then be tested with respect to stiffness and strength, other than geometric accuracy. In relation to this point, the energy required to deform the plate could be computed with the method presented in [20] by considering angular springs between tiles. Finally, the problem of actuating origami structures has been often addressed in the literature, and several solutions are available, such as light, magnetic, electric, swelling, motor, thermal actuation (see the review article [21]), which could be adopted also in the present case by taking advantage of the one-degree-of-freedom property.

Data accessibility. The codes and data used in the paper are available from the Github repository: https://github.com/mpsita/TiledPlates1DOF.git [22].

Declaration of AI use. We have not used AI-assisted technologies in creating this article.

Authors' contributions. F.A.S.: conceptualization, data curation, investigation, methodology, validation, visualization, writing—original draft, writing—review and editing; A.F.: conceptualization, formal analysis, investigation, methodology, validation, visualization, writing—original draft, writing—review and editing; A.M.:

Downloaded from https://royalsocietypublishing.org/ on 27 February 2024

conceptualization, investigation, methodology, validation, writing—original draft, writing—review and editing; R.P.: conceptualization, formal analysis, investigation, methodology, validation, visualization, writing—original draft, writing—review and editing; M.P.S.: conceptualization, formal analysis, investigation, methodology, validation, visualization, writing—original draft, writing—review and editing.

All authors gave final approval for publication and agreed to be held accountable for the work performed therein.

Conflict of interest declaration. We declare we have no competing interests.

Funding. F.A.d.S. acknowledges the Fundação para a Ciência e a Tecnologia (FCT) in the framework of project UIDB/04625/2020 and also the precious help provided by Hugo B. Rebelo and Academia Militar, during the 3D scanning of the plates. R.P. and M.P.S. acknowledge the support from the University of Pisa through the project PRA2022-69 'Advanced modelling of ultra-lightweight materials and structures'. M.P.S. is also supported by the project PRIN 2022-20229BM9EL 'NutShell'. A.F. acknowledges the support from Sapienza University of Rome through the research project 2022 'Mechanics of thin structures and 2D materials: advanced models and new applications'. A.M. acknowledges the funding received in the framework of the project 'OPTYMA - Optimized tensegrity metamaterials', grant no. E83C22002290005, of the University of Rome Tor Vergata.

Acknowledgements. This work has been written within the activities of INdAM-GNFM.

References

1. dos Santos Filipe A, Favata Antonino, Micheletti Andrea, Paroni Roberto, Picchi Scardaoni Marco. 2024 Programming quadric metasurfaces via infinitesimal origami maps of monohedral hexagonal tessellations: Part I. *Proc. R. Soc. A* **480**, 20230430. (doi:10.1098/rspa.2023.0430)
2. Reinhardt K. 1918 *Uber die Zerlegung der Ebene in Polygone*. PhD thesis, Universitat Frankfurt am Main.
3. Bollobas B. 1963 Filling the plane with congruent convex hexagons without overlapping. *Ann. Univ. Sci. Budapest* **6**, 117–123.
4. Al-Tamimi AA, Huang B, Vyas C, Hernández M, Peach C, Bártolo P. 2019 Topology optimised metallic bone plates produced by electron beam melting: a mechanical and biological study. *Int. J. Adv. Manuf. Technol.* **104**, 195–210. (doi:10.1007/s42242-020-00066-8)
5. Vijayavenkataraman S, Gopinath A, Lu W. 2020 A new design of 3D-printed orthopedic bone plates with auxetic structures to mitigate stress shielding and improve intra-operative bending. *Bio-Design Manuf.* **3**, 98–108. (doi:10.1007/s00170-019-03866-0)
6. Kapnisi M *et al.* 2018 Auxetic cardiac patches with tunable mechanical and conductive properties toward treating myocardial infarction. *Adv. Funct. Mater.* **28**, 1800618. (doi:10.1002/adfm.201800618)
7. Khalid S, Raouf I, Khan A, Kim N, Kim HS. 2019 A review of human-powered energy harvesting for smart electronics: recent progress and challenges. *Int. J. Precis. Eng. Manuf.-Green Tech.* **6**, 821–851. (doi:10.1007/s40684-019-00144-y)
8. Moroney C, Alderson A, Allen T, Sanami M, Venkatraman P. 2018 The application of auxetic material for protective sports apparel. *Proceedings* **2**, 251. (doi:10.3390/proceedings2060251)
9. Li Q, Kuang Y, Zhu M. 2017 Auxetic piezoelectric energy harvesters for increased electric power output. *AIP Adv.* **7**, 015104. (doi:10.1063/1.4974310)
10. Ferguson WJG, Kuang Y, Evans KE, Smith CW, Zhu M. 2018 Auxetic structure for increased power output of strain vibration energy harvester. *Sensors Actuat. A: Phys.* **282**, 90–96. (doi:10.1016/j.sna.2018.09.019)
11. Yuan M, Cao Z, Luo J, Chou X. 2019 Recent developments of acoustic energy harvesting: a review. *Micromachines* **10**, 48. (doi:10.3390/mi10010048)
12. Shuyi L, Fan Y, Liu Y, Niu S, Han Z, Ren L. 2021 Smart bionic surfaces with switchable wettability and applications. *J. Bionic Eng.* **18**, 473–500. (doi:10.1007/s42235-021-0038-7)
13. Costa H, Schille J, Rosenkranz A. 2021 Tailored surface textures to increase friction - a review. *Friction* **10**, 1285–1230. (doi:10.1007/s40544-021-0589-y)
14. Miranda R, Babilio E, Singh N, Santos F, Fraternali F. 2020 Mechanics of smart origami sunscreens with energy harvesting ability. *Mech. Res. Commun.* **105**, 103503. (doi:10.1016/j.mechrescom.2020.103503)

15. Nam S, Park S, Yun S, Park B, Park SK, Kyung KU. 2016 Structure modulated electrostatic deformable mirror for focus and geometry control. *Opt. Express* **24**, 55–66. (doi:10.1364/OE.24.000055)
16. Wang Z, Liao D, Zhang T, Chen T, Ruan Y, Zheng B. 2019 Metasurface-based focus-tunable mirror. *Opt. Express* **27**, 30 332–30 339. (doi:10.1364/OE.27.030332)
17. Zhang J, Shaw AD, Wang C, Gu H, Amoozgar M, Friswell MI, Woods BK. 2021 Aeroelastic model and analysis of an active camber morphing wing. *Aerosp. Sci. Technol.* **111**, 106534. (doi:10.1016/j.ast.2021.106534)
18. Jacobsen JO, Chen G, Howell LL, Magleby SP. 2009 Lamina Emergent Torsional (LET) Joint. *Mechanism and Machine Theory* **44**, 2098–2109. (doi:10.1016/j.mechmachtheory.2009.05.015)
19. Wang K, Chang YH, Chen Y, Zhang C, Wang B. 2015 Designable dual-material auxetic metamaterials using three-dimensional printing. *Mater. Des.* **67**, 159–164. (doi:10.1016/j.matdes.2014.11.033)
20. dos Santos FA, Favata A, Micheletti A, Paroni R. 2021 Design of auxetic plates with only one degree of freedom. *Extreme Mech. Lett.* **42**, 101091. (doi:10.1016/j.eml.2020.101091)
21. Leanza S, Wu S, Sun X, Qi HJ, Zhao RR. 2023 Active materials for functional origami. *Adv. Mater.* 2302066. (doi:10.1002/adma.202302066)
22. dos Santos FA, Favata A, Micheletti A, Paroni R, Picchi Scardaoni M. 2024 Programming quadric metasurfaces via infinitesimal origami maps of monohedral hexagonal tessellations - codes and data. Github repository. (https://github.com/mpsita/TiledPlates1DOF.git)

Downloaded from https://royalsocietypublishing.org/ on 27 February 2024